

A Fast Time Splitting Finite Difference Approach to Gross–Pitaevskii Equations

Marco Caliari^{1,*} and Simone Zuccher¹

¹ Department of Computer Science, University of Verona, Italy.

Received 9 July 2020; Accepted (in revised version) 26 October 2020

Abstract. We propose an idea to solve the Gross–Pitaevskii equation for dark structures inside an infinite constant background density $\rho_\infty = |\psi_\infty|^2$, without the introduction of artificial boundary conditions. We map the unbounded physical domain \mathbb{R}^3 into the bounded domain $(-1,1)^3$ and discretize the rescaled equation by equispaced 4th-order finite differences. This results in a free boundary approach, which can be solved in time by the Strang splitting method. The linear part is solved by a new, fast approximation of the action of the matrix exponential at machine precision accuracy, while the nonlinear part can be solved exactly. Numerical results confirm existing ones based on the Fourier pseudospectral method and point out some weaknesses of the latter such as the need of a quite large computational domain, and thus a consequent critical computational effort, in order to provide reliable time evolution of the vortical structures, of their reconnections, and of integral quantities like mass, energy, and momentum. The free boundary approach reproduces them correctly, also in finite subdomains, at low computational cost. We show the versatility of this method by carrying out one- and three-dimensional simulations and by using it also in the case of Bose–Einstein condensates, for which $\psi \rightarrow 0$ as the spatial variables tend to infinity.

AMS subject classifications: 65M06, 65M70

PACS: 67.85.-d, 03.75.-b

Key words: Gross–Pitaevskii boundary conditions, dark structures, vortex rings, unbounded domain, nonlinear Schrödinger equation, fast matrix exponential.

1 Introduction

The nonlinear (cubic) Schrödinger equation with external potential

$$i\frac{\partial\psi}{\partial t}(x,t) + a\nabla^2\psi(x,t) - V(x)\psi(x,t) + s|\psi(x,t)|^2\psi(x,t), \quad x \in \mathbb{R}^3, \quad (1.1)$$

*Corresponding author. Email addresses: marco.caliari@univr.it (M. Caliari), simone.zuccher@univr.it (S. Zuccher)

where ψ is the complex wavefunction, $a > 0$ and $s \in \mathbb{R}$, is commonly used as a model for the dynamics of Bose–Einstein condensates (BECs, see [3] for a review of the mathematical theory and numerical methods) and of superfluids (see [6,21] for the derivation of such an equation). In both cases, it is also known as Gross–Pitaevskii equation (GPE). From the mathematical point of view, one of the main differences between BECs and superfluid simulations is in the boundary conditions satisfied by the wavefunction ψ . In the first case they are vanishing, that is $\psi \rightarrow 0$ as $|x| \rightarrow \infty$, whereas for superfluids the interest is in the dynamics of dark structures, such as solitons, vortex lines, and vortex rings, which are objects with a core of (near) zero density $\rho = |\psi|^2$ inside an infinite constant background density ρ_∞ . In order to impose the boundary conditions in the former case, the unbounded domain \mathbb{R}^3 is usually truncated and homogeneous Dirichlet or periodic boundary conditions are set. Hence, sine or Fourier pseudospectral discretizations in space can be used. In the latter case, common simple techniques are quite artificial and consist in homogeneous Neumann boundary conditions (see [13]) or periodic boundary conditions, after a proper mirroring of the truncated computational domain (see [13, 17, 23]). Even though the domain has to be doubled in the directions lacking periodicity, the pseudospectral Fourier discretization in space is commonly used because it fits well with the time splitting Fourier pseudospectral (TSFP) method which, in the context of BECs, is the method of choice, due to its simplicity, efficiency (thanks to the Fast Fourier Transform), spectral accuracy in space, and the properties of unconditional stability, time reversibility, gauge invariance, and mass preservation (see [3, § 4.1]). Quite recently, it was proposed in [15] a new simple method, called Modulus Square Dirichlet (MSD), for the treatment of boundary conditions in the form

$$\rho_{|b} = |\psi_{|b}|^2 = B, \quad B > 0, \quad (1.2)$$

where $\psi_{|b}$ denotes the restriction of ψ at the boundaries of a *bounded* domain and B is the value of the modulus square which must be constant both in space and time at the boundaries. For this reason, MSD boundary conditions cannot be used for straight vortices as their density $\rho = |\psi|^2$ is not constant at boundaries that intersect their cores. Overall, the method introduced in [15] is a Runge–Kutta finite difference scheme of order four both in space and time. Other approaches to the solution of the Gross–Pitaevskii equation with non-vanishing boundary conditions are based on the far field asymptotic behavior (see [4]), or on the imposition of inhomogeneous Dirichlet boundary conditions in a truncated domain (see [26,27]). In this paper we propose another simple way to treat this type of boundary conditions. We are concerned with superfluid simulations, for which the GPE takes the form

$$\psi_t = \frac{i}{2} \nabla^2 \psi + \frac{i}{2} (1 - |\psi|^2) \psi. \quad (1.3)$$

It is usually understood to have $\rho = |\psi|^2 = 1$ at infinity (see [6]), although straight vortices are an exception. First of all, we explicitly compute in Section 2 mass, energy and momentum variations over a bounded domain Ω , taking into account the peculiarity of the boundary conditions. In Section 3 we perform a change of variable $\eta(\mathbf{y}, t) = \psi(\mathbf{x}, t)$, so as

to map $x \in \mathbb{R}^3$ to $y \in (-1,1)^3$, and then discretize in space with 4th-order finite differences. The resulting system of ordinary differential equations becomes

$$z'(t) = Az(t) + \frac{i}{2}(1 - |z(t)|^2)z(t), \quad (1.4)$$

where $z(t)$ is a vector of dimension (degree of freedom) $M = m_1 \times m_2 \times m_3$ and m_i is the number of discretization points along the i -th direction. We apply in Section 4 the Strang time splitting to the system above, thus yielding the new method that we call Free Boundary Time Splitting Finite Difference (FBTSFD) method. In particular, we solve the linear part of (1.4) by an efficient approximation of the action of the matrix exponential. Finally, we present in Section 5 several numerical experiments which confirm the flexibility and the reliability of the new proposed method.

2 Time derivatives of mass, energy, and momentum

In this section we state the time derivatives of mass, energy and momentum in a bounded domain Ω in terms of boundary integrals, without any particular assumption on the wavefunction ψ and its derivatives at $\partial\Omega$. We relegate to Appendix A the explicit computations.

2.1 Mass

Mass in a bounded domain $\Omega \subset \mathbb{R}^3$ is defined by

$$m_\Omega(t) = \int_{\Omega} |\psi|^2 dV. \quad (2.1)$$

As shown in Appendix A.1, it is easy to derive

$$m'_\Omega(t) = \Im \left[\int_{\partial\Omega} \psi (\nabla \bar{\psi} \cdot \hat{n}) dS \right], \quad (2.2)$$

where the symbol \Im denotes the imaginary part of a complex quantity. From this we conclude what follows.

If $\psi \rightarrow 0$ at the boundary $\partial\Omega$, then mass is conserved. This is typically the case in which Eq. (1.1) models Bose-Einstein condensates and a spectral Hermite discretization is employed in the unbounded domain Ω (see [25], for instance) or homogeneous Dirichlet boundary conditions are used in a truncated domain.

If $\nabla\psi$ is orthogonal to \hat{n} or vanishing, i.e. $\nabla\bar{\psi} \cdot \hat{n}|_{\partial\Omega} = 0$, then mass is conserved. This is usually the case in which homogeneous Neumann boundary conditions are set in a truncated domain Ω .

If Ω is a computational box and ψ is periodic at opposite boundaries then the right hand side of Eq. (2.2) is zero and mass is conserved. This is the case of the Fourier pseudospectral method in a truncated domain Ω (used to approximate vanishing boundary

conditions) or in a mirrored truncated domain Ω (for non-vanishing boundary conditions).

2.2 Energy

The Hamiltonian energy is defined by

$$E_\Omega(t) = \frac{1}{2} \int_{\Omega} |\nabla \psi|^2 dV + \frac{1}{4} \int_{\Omega} (1 - |\psi|^2)^2 dV. \quad (2.3)$$

As shown in Appendix A.2, the time derivative of the Hamiltonian is

$$E'_\Omega(t) = \Im \left[\frac{1}{2} \int_{\partial\Omega} (\nabla^2 \bar{\psi} + (1 - |\psi|^2) \bar{\psi}) \nabla \psi \cdot \hat{n} dS \right] \quad (2.4)$$

and therefore we have the following cases.

If $\nabla \psi$ is orthogonal to \hat{n} or vanishing, i.e. $\nabla \bar{\psi} \cdot \hat{n}|_{\partial\Omega} = 0$, then energy is conserved.

If Ω is a computational box and ψ is periodic at opposite boundaries then the right hand side of Eq. (2.4) is zero and energy is conserved.

If ψ is constant in time on $\partial\Omega$, energy is conserved because $\nabla^2 \bar{\psi} + (1 - |\psi|^2) \bar{\psi} = 2i\bar{\psi}_t$.

2.3 Momentum

The linear momentum is defined by

$$p_\Omega(t) = \int_{\Omega} \rho \mathbf{u} dV, \quad (2.5)$$

where ρ and \mathbf{u} are the Madelung variables related to the wavefunction by

$$\psi = \sqrt{\rho} e^{iS}, \quad \rho = |\psi|^2, \quad \mathbf{u} = \nabla S. \quad (2.6)$$

As reported in Appendix A.3, the linear momentum can be written in terms of the wavefunction as

$$p_\Omega(t) = \Im \left[\int_{\Omega} \bar{\psi} \nabla \psi dV \right] \quad (2.7)$$

and the time derivative of its ℓ -th component as

$$p'_{\ell\Omega}(t) = -\frac{1}{2} \Re \left[\int_{\partial\Omega} (\psi_{x_\ell} \nabla \bar{\psi} - \bar{\psi} \nabla (\psi_{x_\ell}) + \mathbf{F}_\ell) \cdot \hat{n} dS \right], \quad (2.8)$$

where \Re denotes the real part of a complex quantity and $\mathbf{F}_\ell = |\psi|^4 \hat{e}_\ell / 2$, \hat{e}_ℓ being the unit vector along the ℓ -th direction. Similarly to mass and energy, we have the following cases.

If ψ and its gradient tend to zero at $\partial\Omega$ then the linear momentum is conserved.

If Ω is a computational box and ψ is periodic at opposite boundaries then the right hand side of Eq. (2.8) is zero and momentum is conserved.

If $|\psi|^2 \rightarrow B$ and $\nabla \psi \rightarrow 0$ at $\partial\Omega$, then the linear momentum is conserved.

3 Space scaling and discretization

When the Gross–Pitaevskii equation (1.3) models the time evolution of dark structures then background density ρ_∞ typically tends to 1 at infinity. In contrast to other approaches which try to move the conditions from infinity to the boundaries of a truncated computational domain (see Section 1 and references therein), we prefer to use a *mapping* method [7, § 17.6] to rescale the space variable and leave away the boundary constraints.

Let $x = (x_1, x_2, x_3)$. We wish to rewrite the GPE (1.3) in terms of $\eta(y, t) = \psi(x, t)$, where $y = (y_1, y_2, y_3)$ and $y_i: (-\infty, +\infty) \rightarrow (-1, 1)$ for $i = 1, 2, 3$. The Laplacian operator then becomes

$$\nabla^2 \psi = \sum_{\ell=1}^3 \frac{\partial^2 \psi}{\partial x_\ell^2} = \sum_{\ell=1}^3 \left(y_\ell'^2 \frac{\partial^2 \eta}{\partial y_\ell^2} + y_\ell'' \frac{\partial \eta}{\partial y_\ell} \right),$$

and the GPE (1.3) can be rewritten as

$$\eta_t = \frac{i}{2} \left(\sum_{\ell=1}^3 y_\ell'^2 \frac{\partial^2 \eta}{\partial y_\ell^2} + y_\ell'' \frac{\partial \eta}{\partial y_\ell} \right) + \frac{i}{2} (1 - |\eta|^2) \eta. \quad (3.1)$$

A possible choice of the function y_ℓ is

$$y_\ell(x_\ell) = \frac{2}{\pi} \arctan \left(\frac{x_\ell}{\alpha_\ell} \right) \iff x_\ell(y_\ell) = \alpha_\ell \tan \left(\frac{\pi}{2} y_\ell \right), \quad \alpha_\ell > 0 \quad (3.2)$$

from which we get

$$\begin{aligned} y'_\ell(x_\ell) &= \frac{2\alpha_\ell}{\pi(x_\ell^2 + \alpha_\ell^2)} = \frac{2}{\pi\alpha_\ell (\tan^2(\frac{\pi}{2}y_\ell) + 1)}, \\ y''_\ell(x_\ell) &= -\frac{4\alpha_\ell x_\ell}{\pi(x_\ell^2 + \alpha_\ell^2)^2} = -\frac{4\tan(\frac{\pi}{2}y_\ell)}{\pi\alpha_\ell^2 (\tan^2(\frac{\pi}{2}y_\ell) + 1)^2}. \end{aligned}$$

Other choices are possible, in particular we tested the so-called *logarithmic* map [7, formula (17.33)]

$$y_\ell(x_\ell) = \tanh \left(\frac{x_\ell}{\alpha_\ell} \right) \iff x_\ell(y_\ell) = \alpha_\ell \operatorname{arctanh}(y_\ell), \quad (3.3)$$

from which we get

$$\begin{aligned} y'_\ell(x_\ell) &= \frac{1}{\alpha_\ell} \left(1 - \tanh^2 \left(\frac{x_\ell}{\alpha_\ell} \right) \right) = \frac{1 - y_\ell^2}{\alpha_\ell}, \\ y''_\ell(x_\ell) &= -\frac{2}{\alpha_\ell^2} \tanh \left(\frac{x_\ell}{\alpha_\ell} \right) \left(1 - \tanh^2 \left(\frac{x_\ell}{\alpha_\ell} \right) \right) = -\frac{2}{\alpha_\ell^2} y_\ell (1 - y_\ell^2), \end{aligned}$$

but we obtained overall better numerical results with (3.2), see for instance the experiments in Section 5.4.1. We notice that for a given parametrized mapping, the accuracy of the solution might depend on the choice of the parameter itself.

3.1 Discretization by fourth order finite differences

We consider an *inner* discretization of the space with one-sided finite differences close to the boundaries. This approach is similar to the one denominated 1SD in [15], but it is here employed in the bounded *transformed* domain, not in a *truncated* domain. For the convenience of the reader, we describe the discretization in one dimension. The interval $(-1,1)$ is discretized with m_ℓ points Y_ℓ^j , $j = 1, 2, \dots, m_\ell$, where $Y_\ell^j = -1 + 2j/(m_\ell + 1)$. The first and second derivative operators are discretized with central finite differences of the fourth order if enough surrounding points are available, with one-sided finite differences otherwise. We report here the corresponding one-dimensional discretization matrix for the first derivative

$$\delta_{y_\ell} = \frac{1}{K_\ell} \begin{bmatrix} -\frac{25}{12} & 4 & -3 & \frac{4}{3} & -\frac{1}{4} \\ -\frac{1}{4} & -\frac{5}{6} & \frac{3}{2} & -\frac{1}{2} & \frac{1}{12} \\ -\frac{1}{12} & \frac{2}{3} & 0 & -\frac{2}{3} & \frac{1}{12} \\ \ddots & \ddots & \ddots & \ddots & \ddots \\ -\frac{1}{12} & \frac{2}{3} & 0 & -\frac{2}{3} & \frac{1}{12} \\ -\frac{1}{12} & \frac{1}{3} & -\frac{3}{2} & -\frac{3}{2} & \frac{1}{12} \\ \frac{1}{4} & -\frac{4}{3} & 3 & -4 & \frac{25}{12} \end{bmatrix},$$

and for the second derivative

$$\delta_{y_\ell^2} = \frac{1}{K_\ell^2} \begin{bmatrix} -\frac{15}{4} & -\frac{77}{6} & \frac{107}{6} & -13 & \frac{61}{12} & -\frac{5}{6} \\ -\frac{5}{6} & -\frac{4}{3} & -\frac{5}{3} & \frac{7}{3} & -\frac{1}{2} & \frac{1}{12} \\ -\frac{1}{12} & \frac{1}{3} & -\frac{5}{2} & \frac{4}{3} & -\frac{1}{12} & \\ \ddots & \ddots & \ddots & \ddots & \ddots & \\ \frac{1}{12} & -\frac{1}{12} & \frac{4}{3} & -\frac{5}{2} & -\frac{4}{3} & -\frac{1}{12} \\ -\frac{5}{6} & \frac{61}{12} & -13 & \frac{107}{6} & -\frac{77}{6} & \frac{15}{4} \end{bmatrix},$$

where $K_\ell = 2/(m_\ell + 1)$ is the spatial grid size in the rescaled domain. Point Y_ℓ^j corresponds, through Eq. (3.2), to a point X_ℓ^j in the physical unbounded domain, where the discretization is non-uniform and the grid step size in the ℓ -th direction is $H_\ell^j = X_\ell^{j+1} - X_\ell^j$. The set of discretization points in the rescaled domain is denoted by $Y \subset (-1,1)^3$. The final matrix corresponding to the discretization of the linear part of Eq. (3.1) is $A \in i\mathbb{R}^{M \times M}$, $M = m_1 \times m_2 \times m_3$ and it is obtained by simple Kronecker products of the one-dimensional matrices. In fact, we have

$$A = I_{m_3} \otimes I_{m_2} \otimes A_1 + I_{m_3} \otimes A_2 \otimes I_{m_1} + A_3 \otimes I_{m_2} \otimes I_{m_1}, \quad (3.4)$$

where I_{m_ℓ} is the identity matrix of dimension m_ℓ ,

$$A_\ell = \frac{i}{2} \left(\text{diag}([y'_\ell(X_\ell^j)^2]_j) \delta_{y_\ell^2} + \text{diag}([y''_\ell(X_\ell^j)]_j) \delta_{y_\ell} \right),$$

and $\text{diag}([w_j]_j)$ denotes the diagonal matrix with the vector $[w_j]_j$ in its diagonal.

4 Numerical time integration

The time splitting finite difference (TSFD) method is well established for the time integration of (1.4). It relies on the composition of the solutions of the two parts

$$u'(t) = Au(t), \quad (4.1a)$$

$$v'(t) = \frac{i}{2} (1 - |v(t)|^2) v(t). \quad (4.1b)$$

For the solution of the linear equation (4.1a), we directly approximate the exact solution

$$u_{n+1} = \exp(\tau A) u_n, \quad u_n \approx u(t_n).$$

Taking into account the particular structure of the matrix, it is possible to write

$$\exp(\tau A) u = \exp(\tau A_3) \otimes \exp(\tau A_2) \otimes \exp(\tau A_1) u,$$

where u is a general complex column vector of length M . Although the problem of computing the exponential of a large matrix τA is reduced to the approximation of much smaller matrix exponentials $\exp(\tau A_\ell)$, the formula above cannot be used because the Kronecker product of the three matrix exponentials is a full matrix of dimension $M \times M$. We consider instead the three-dimensional tensor $\mathbf{U} = (u_{i_1, i_2, i_3}) \in \mathbb{C}^{m_1 \times m_2 \times m_3}$ which corresponds to the vector u through the relation

$$u_{i_1, i_2, i_3} = u_{i_1 + m_1(i_2 - 1) + m_1 m_2(i_3 - 1)}.$$

The relation above is denoted by $\text{vec}(\mathbf{U}) = u$, too. By setting $E_\ell = \exp(\tau A_\ell)$, $E_\ell = (e_{i_\ell, j_\ell}^\ell)$, and performing elementary calculations it is possible to write

$$\exp(\tau A) u = \text{vec}(\mathbf{V}) = \text{vec}((v_{i_1, i_2, i_3})) = \text{vec} \left(\sum_{j_1, j_2, j_3} u_{j_1, j_2, j_3} e_{i_1, j_1}^1 e_{i_2, j_2}^2 e_{i_3, j_3}^3 \right),$$

but the direct implementation requires three nested loops which are quite inefficient in interpreted languages like MATLAB[†]. The routine `ndcovlt`[‡] (available in the package described in [12]) performs the same three-dimensional covariant linear transform avoiding the loops. Moreover, the three small matrices E_ℓ can be computed once and for all by standard methods like Padé or Taylor approximations. The MATLAB function `expm`, for instance, guarantees an approximation of $\exp(\tau A_\ell)$ in a backward stable way, independently of the norm (and thus of the stiffness) of the matrix. This is made possible by an optimal choice of the order of the Padé approximation in combination with the number of steps in the underlying scaling and squaring algorithm, see [2]. The same is true for the

[†]We refer to MATLAB as the language interpreted by softwares like Matlab® and GNU Octave.

[‡]Originally written by Jaroslav Hajek for the linear-algebra package of GNU Octave.

Taylor method described in [11], which computes the matrix exponential up to machine precision, as well.

The solution of the nonlinear equation (4.1b) is trivial, since $|v(t)|$ is preserved by the equation. Therefore

$$v(t_{n+1}) = v_{n+1} = \exp(\text{diag}\{\tau d_n\}) v_n, \quad v_n \approx v(t_n),$$

where $\text{diag}\{\tau d_n\}$ denotes the diagonal matrix with diagonal

$$\tau d_n = \tau \frac{i}{2} (1 - |v_n|^2).$$

From the implementation point of view, no matrix has to be created, since it is enough to perform the component-wise exponentiation $\exp(\tau d_n)$ and multiplication by v_n . This property can be used to work directly with the tensor V_n such that

$$\text{vec}(V_n) = v_n.$$

The solution of the whole equation (1.4) is eventually recovered by the so-called Strang splitting (see, for instance, [3]), which is a method of order two with respect to τ . Higher order splitting methods would be possible (we refer to [25] for numerical experiments in BECs), as well as other time integrators.

Time splitting methods are usually preferred to classical explicit methods, such as Runge–Kutta type, since in general they preserve the mass, are time-reversible, gauge invariant, and unconditionally stable. In our case, the matrix A is not skew-Hermitian and therefore $\|u_{n+1}\|_2 = \|\exp(\tau A)u_n\|_2 \neq \|u_n\|_2$. This means that the discrete mass, related to $\|u_n\|_2^2$, is not conserved by this step, and the error depends on the space discretization (being the time integration exact).

Remark 4.1. In the time splitting Fourier pseudospectral method, the first part (4.1a) is written as

$$\frac{\partial u}{\partial t}(x, t) = i \frac{\nabla^2}{2} u(x, t),$$

the solution is approximated by a truncated Fourier series and solved thanks to the Fast Fourier Transform (FFT). If the initial solution $\psi_0(x)$ is not periodic along one or more directions in the bounded domain $\Omega = [x_{1\min}, x_{1\max}] \times [x_{2\min}, x_{2\max}] \times [x_{3\min}, x_{3\max}]$, then it is mirrored along those directions, in order to take at least the same values at opposite boundaries. This implies a higher computational effort and larger memory requirements.

5 Numerical experiments

5.1 Initial conditions

The only nontrivial time-independent solution of Gross–Pitaevskii equation (1.3) is the straight vortex, whose two-dimensional numerical approximation can be computed quite

easily and for which high-order Padé approximations exist [13]. Thus, the straight vortex can be used as the initial condition to test the correctness of a new code (see Section 5.2). However, any other type of vortex line such as vortex rings or torus knots [23, 31] require *ad hoc* techniques [19]. In general, if more than a vortex is present, each complex wavefunction ψ_i corresponding to the i -th vortex line is computed separately and then the global initial wavefunction ψ is obtained by multiplying all ψ_i as first done in [17].

For the single straight vortex we use the 4th-order Padé approximation introduced in [13] and make the phase S change by 2π in a plane orthogonal to the vortex.

For any other configuration made of a single closed loop or multiple vortices we first employ the Biot–Savart integral to compute the velocity field $\mathbf{u}(x)$ induced by the system of vortices at each position x of the domain $\Omega \subseteq \mathbb{R}^3$ and then we integrate the equation $\mathbf{u} = \nabla S$ (see (2.6)) to get the phase $S(x)$. Once a reference value S_0 is given at a certain point $x_0 \in \Omega$, integration can be performed along any direction. This idea was used in [23]. We tried to apply it as described in the paper, but we encountered many numerical problems when integrating close to the vortex centerline because *phase is not defined on* the vortex centerline as quantum vortices are phase defects [5]. In order to overcome this issue, we first choose a point in the bulk of the domain, sufficiently far from any vortex, where we set $S=0$. From that point we extend the integration sufficiently far from the vortex tangle, avoiding points whose distance from the vortex centerline is below a certain reference value. Once S has been computed away from vortex centerlines, we extend the integrals moving closer to the vortex lines and moving away toward the boundaries. *A posteriori* checks of ∇S show very good agreement with the velocity field \mathbf{u} generated using Biot–Savart integral. As far as the absolute value of the initial wavefunction is concerned, $|\psi| = \sqrt{\rho}$, we choose to assign the density ρ at each point of the domain according to the 4th-order Padé approximation of the steady straight vortex. This is the correct value of density only for the case of a single straight vortex, thus it is not guaranteed to be the correct one for any other case. Nevertheless, it is commonly accepted by authors [19, 23, 31] in this field of research. Since $\rho = \rho(r)$, for each grid point we chose r as the minimum distance from the closest vortex centerlines.

This approach is very time consuming because of the Biot–Savart integral. In the case of a single vortex ring, whose dynamics is very well known in different classical fluids (viscous or inviscid, incompressible or compressible flows) [1, 24] and in quantum fluids [20, 22], one can resort to a more *naive* and fast approach as done in [30].

Table 1 compares the “measured” velocity U_m of vortex rings of different radii R deduced from the numerical simulations with the theoretical values in a Bose condensate computed according to [22]

$$U = \frac{\kappa}{4\pi R} \left[\ln\left(\frac{8R}{a}\right) - 0.615 \right], \quad (5.1)$$

where κ is the quantum of circulation and $a = \xi$ is the healing length, whose values in our case are respectively $\kappa = 2\pi$ and $\xi = 1$. From the relative errors reported in the last column of Table 1 we conclude that the velocity of the vortex rings generated according to the

Table 1: Speed of a moving vortex ring, comparison with theoretical values in a Bose condensate as reported in [22] for different radii R . The first three lines refer to the initial condition here described and based on the Biot-Savart integral, the last three lines refer to the initial condition used in [30].

	U_m	U	$ U_m/U - 1 $
$R=8$	$2.20 \cdot 10^{-1}$	$2.21 \cdot 10^{-1}$	$8.71 \cdot 10^{-3}$
$R=16$	$1.31 \cdot 10^{-1}$	$1.32 \cdot 10^{-1}$	$1.29 \cdot 10^{-2}$
$R=24$	$9.41 \cdot 10^{-2}$	$9.67 \cdot 10^{-2}$	$2.71 \cdot 10^{-2}$
$R=8$, Ref. [30]	$1.78 \cdot 10^{-1}$	$2.21 \cdot 10^{-1}$	$1.97 \cdot 10^{-1}$
$R=16$, Ref. [30]	$8.39 \cdot 10^{-2}$	$1.32 \cdot 10^{-1}$	$3.66 \cdot 10^{-1}$
$R=24$, Ref. [30]	$5.55 \cdot 10^{-2}$	$9.67 \cdot 10^{-2}$	$4.26 \cdot 10^{-1}$

approach here described are in remarkable agreement with the theoretical predictions with errors below 2%, whereas more *naive* approaches to the initial condition lead to quite poor results. For more details on self-preserving vortex rings see [28].

5.2 Preservation of the stationary straight vortex

In the first set of numerical experiments we check the preservation of the stationary straight vortex centered in $(0,0)$ in the plane x_1Ox_2 and parallel to x_3 . The corresponding wavefunction (constant along x_3) is

$$\psi_0(x_1, x_2, x_3) = \rho(r)^{1/2} e^{i\theta},$$

where $r = \sqrt{x_1^2 + x_2^2}$, $\theta = \arg(x_1 + ix_2)$ and $\rho(r)$ is the 4-th order Padé approximation of the solution of the differential equation

$$\rho'' + \frac{\rho'}{r} - \frac{(\rho')^2}{2\rho} - \frac{2\rho}{r^2} + 2(1-\rho)\rho = 0,$$

with $\rho(0) = 0$ and $\rho(r \rightarrow \infty) = 1$ (see [13]). Although it is a stationary solution of (1.3), there are three sources of perturbation when it comes to the numerical integration: the approximation by a rational function of $\rho(r)$, the discretization of the space derivatives and the time splitting method. We check the correctness of the convergence rate of the finite differences and the time integrator. First of all, we fix the time step size $\tau = 1/35$ and consider different spatial discretizations in the transformed domain $(-1,1)^3$ according to (3.2) with $\alpha = (5,5,5)$, using $M = m_1 \times m_2 \times 11$ discretization points, where $m_1 = m_2$ ranges from 23 to 63. We compute the maximum pointwise relative error

$$\max_{y \in Y_0} \frac{|\eta_n(y) - \eta_0(y)|}{|\eta_0(y)|}, \quad Y_0 = Y \setminus \{0\}, \quad \eta_n(y) \approx \psi(x, t_n) \quad (5.2)$$

at $t_n = 1$. In Fig. 1, left, we observe the correct fourth order spatial convergence rate. Then, we fix $M = 87 \times 87 \times 11$ and let the time step τ to range from $1/10$ to $1/25$. We observe in Fig. 1, right, the correct second order time convergence rate.

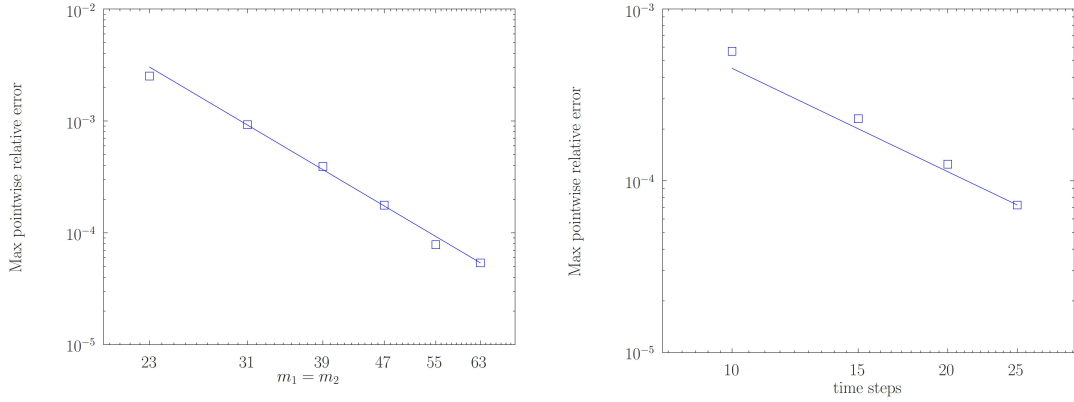


Figure 1: Maximum pointwise relative error (5.2) at $t_n=1$ with $\tau=1/35$ and varying number of discretization points $M=m_1 \times m_2 \times 11$ (left), and $M=87 \times 87 \times 11$ and varying number of time steps $1/\tau$ (right).

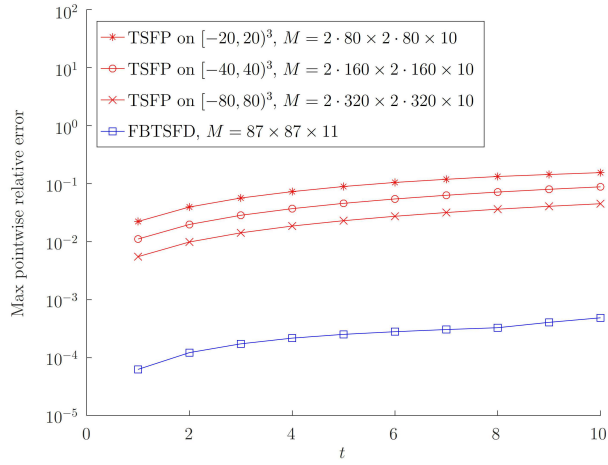


Figure 2: Behavior of the relative error in maximum norm (5.2) for the TSFP (red lines) and the FBTSFD method (blue line).

We perform then an experiment similar to that described in [13, § 4.1], by considering a spatial discretization in the transformed domain $(-1,1)^3$ with $M=87 \times 87 \times 11$ points with $\alpha=(5,5,5)$. This corresponds to a discretization in the physical domain $(-\infty, +\infty)^3$ in which the smallest spatial grid size is about $1.8 \cdot 10^{-1}$ and the average spatial grid size in $(-20,20)$ is about $5.3 \cdot 10^{-1}$ in directions x_1 and x_2 . The rough discretization in x_3 direction does not affect the results, since the straight vortex is constant (both in space and time) along x_3 . The time step size is $\tau=0.002$ and we measure the maximum pointwise relative error (5.2) at $t_n=1, 2, \dots, 10$, respectively. In Fig. 2 we compare the result with the standard time splitting Fourier pseudospectral (TSFP) method, as implemented in [12].

Table 2: Degrees of freedom and elapsed computational times for the experiment on the preservation of the stationary straight vortex.

method	d.o.f.	CPU time (s.)
FBTSFD	$87 \times 87 \times 11$	14.39
TSFP	$2 \cdot 80 \times 2 \cdot 80 \times 10$	20.27
TSFP	$2 \cdot 160 \times 2 \cdot 160 \times 10$	113.81
TSFP	$2 \cdot 320 \times 2 \cdot 320 \times 10$	606.73

The domain is $[-20, 20]^3$, with mirrored x_1 and x_2 directions and discretized with $M = 2 \cdot 80 \times 2 \cdot 80 \times 10$ points. We also consider the same method in the domain $[-40, 40]^3$ and $M = 2 \cdot 160 \times 2 \cdot 160 \times 10$ discretization points and domain $[-80, 80]^3$ with $M = 2 \cdot 320 \times 2 \cdot 320 \times 10$ discretization points. The errors are measured in the interior of the corresponding domains.

We observe in Fig. 2 that the Free Boundary Conditions Time Splitting Finite Difference (FBTSFD) method is far more accurate than TSFP method in which the errors clearly depends on the artificial periodic boundary conditions imposed in the mirrored domain. In fact, when the size of the physical domain is increased by preserving the same space discretization quality, the error becomes smaller. We report in Table 2 the elapsed computational times on a laptop with 12 cores running Matlab® R2019a. As already mentioned in Section 1, MSD boundary conditions cannot be used in this experiment, since the absolute value of the wavefunction is not constant at the boundaries of type $|x_3| = \text{const}$. However, they could be applied in the $x_1 O x_2$ domain, coupled with other boundary conditions in the x_3 direction (periodic, for instance). This simple idea cannot be implemented in the case of orthogonal straight vortices (see Section 5.3.3).

5.2.1 Stationary straight vortex preservation over long time integration

While performing the tests described above, we observed that for a given spatial discretization there exists a maximum time step τ for which the stationary vortex is numerically preserved. We decided to make an extensive simulation, both for the FBTSFD and the TSFP method in the domain $[-20, 20]^3$. The results are collected in Fig. 3. For different values of spatial grid sizes (corresponding to the different lines) we run the simulation up to the final time $T = 50$ with different time steps (corresponding to the point markers) and checked the maximum pointwise relative error (5.2). In order to make the plot easier to compare with the corresponding case for the TSFP method, we reported the average spatial grid sizes (denoted by \bar{H}_1 and \bar{H}_2) in the x_1 and x_2 dimensions of the unbounded domain for the FBTSFD method and the uniform spatial grid sizes (simply denoted by H_1 and H_2) for the TSFP one. For both methods (top plots), we clearly observe that the straight vortex is well preserved up to a maximum time step τ which decreases with the decreasing of the (average) spatial grid size. Thereafter, the error line immediately jumps. In these cases, the density and the phase of the wavefunction do not resemble anymore

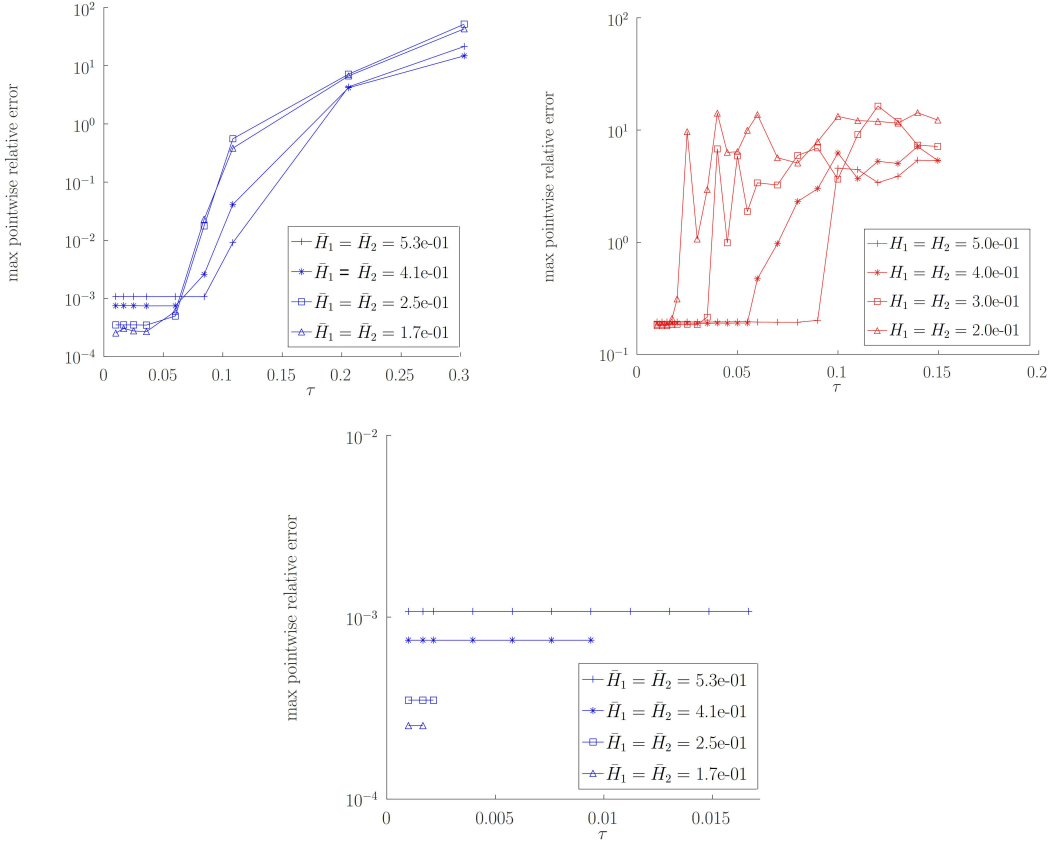


Figure 3: Stationary straight vortex preservation up to $T=50$ with the FBTSFD method (top left), TSFP (top right), and the free boundary condition approach and 4th-order Runge–Kutta time integrator (bottom).

those of a vortical structure. For the FBTSFD method it is also clear that the preservation error depends on the space discretization and, when it is below 10^{-2} , it decreases with the size of the spatial grid size (top left plot). For the TSFP method, since the preservation error mostly depends on the artificial boundary conditions, we see that it does not decrease with the spatial grid size $H_1 = H_2$ (top right plot).

For this experiment we consider also the classical 4th-order Runge–Kutta method (see [15]). In this case the method is conditionally stable and there is a maximum allowed time step. Exceeding it makes the solution to diverge to infinity. The errors corresponding to working time steps are shown in Fig. 3 (bottom plot). The maximum allowed time steps are smaller than those in the Strang splitting scheme. To give an example, the maximum allowed time step for the discretization corresponding to $\bar{H}_1 = \bar{H}_2 = 1.7 \cdot 10^{-1}$ ($M=279 \times 279 \times 11$) is $1.7 \cdot 10^{-3}$ for the Runge–Kutta method and it is $3.6 \cdot 10^{-2}$ when using the Strang splitting scheme. The normalized (with respect to FBTSFD) elapsed time for the Runge–Kutta method is 2.6.

5.3 Full three-dimensional simulations

5.3.1 Comparison with some available results

In Figs. 4–7 we present the dynamics of two rings linked together as done in [30] and compare vortex tubes (isosurfaces at $\rho = 0.02$) obtained with the Fourier approach [30] (left) versus the present one (center). The plot on the left refers to a spatial domain $\Omega = [-20,30] \times [-25,25] \times [-20,30]$ with a spatial resolution $\xi/3$ (ξ being the healing length), i.e. there are 150^3 degrees of freedom in the physical domain, which become 8×150^3 in the computational domain due to mirroring in each spatial direction. The time step is $\tau = 1/80 = 0.0125$. At $t = 0$ the two rings of radius $R = 8$ are placed on mutually orthogonal planes centered at $(0.5, 4.5, 0)$ in the plane $x_3 = 0$, and at $(0, -4, 0)$ in the plane $x_1 = 0$. Present results, shown in the central plot, are obtained with an *average spatial resolution* $\bar{H}_i = 0.4$ within the box $[-20,20]^3$ (moving towards infinity the spatial resolution decreases). This is achieved with $\alpha_i = 15$ in each direction and 171^3 degrees of freedom. The time step is $\tau = 0.02$. These parameters are comparable to those used in [30]. In Figs. 4–7 there is also a plot on the right, which refers to the Fourier approach (as the plot

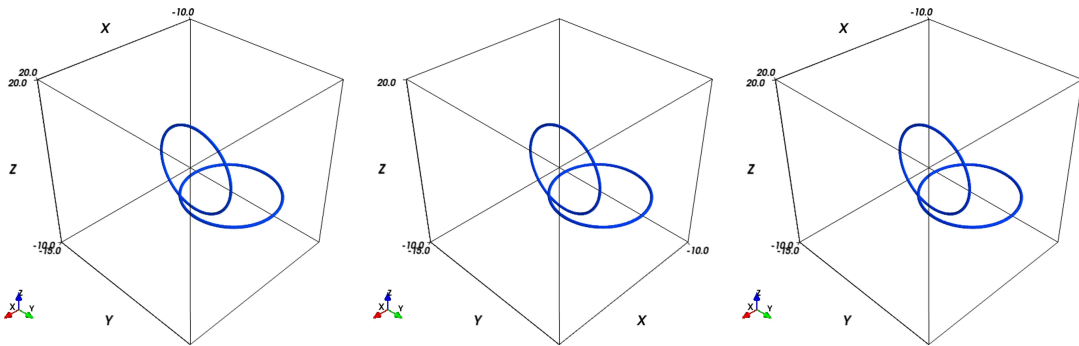


Figure 4: Initial condition as in [30], comparison between TSFP in $\Omega = [-20,30] \times [-25,25] \times [-20,30]$ (left), FBTSFD (center) and TSFP in 2Ω (right) at $t = 0$, $\rho = 0.02$.

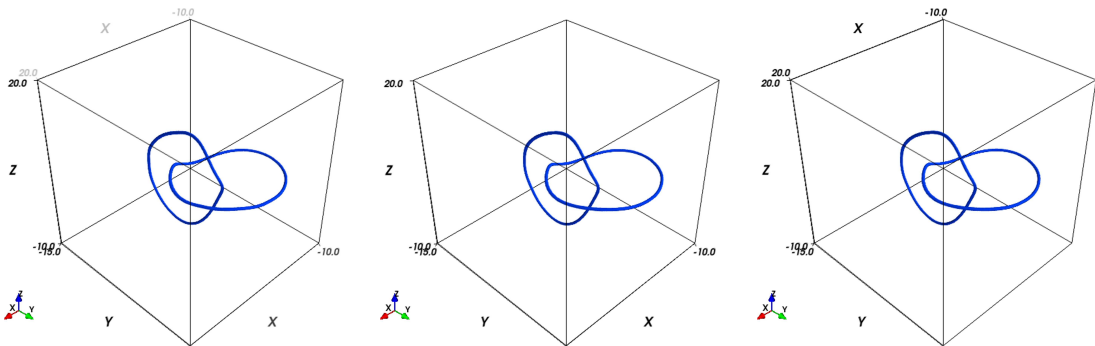


Figure 5: Initial condition as in [30], comparison between TSFP in $\Omega = [-20,30] \times [-25,25] \times [-20,30]$ (left), FBTSFD (center) and TSFP in 2Ω (right) at $t = 20$, $\rho = 0.02$.

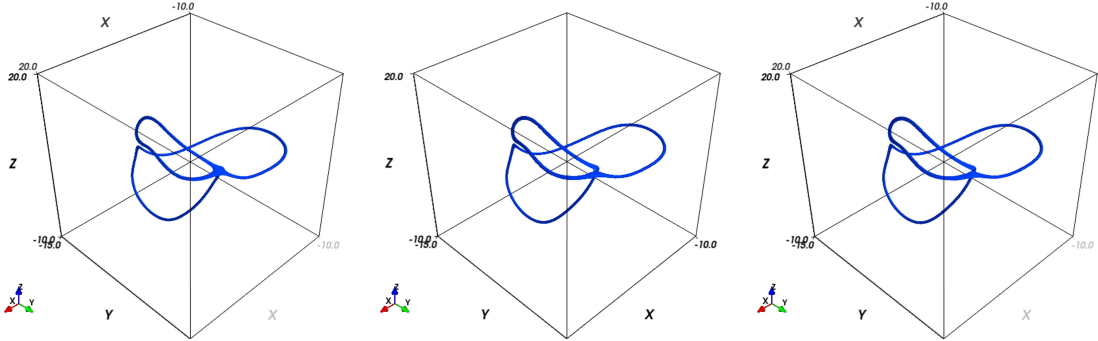


Figure 6: Initial condition as in [30], comparison between TSFP in $\Omega = [-20, 30] \times [-25, 25] \times [-20, 30]$ (left), FBTSFD (center) and TSFP in 2Ω (right) at $t=40$, $\rho=0.02$.

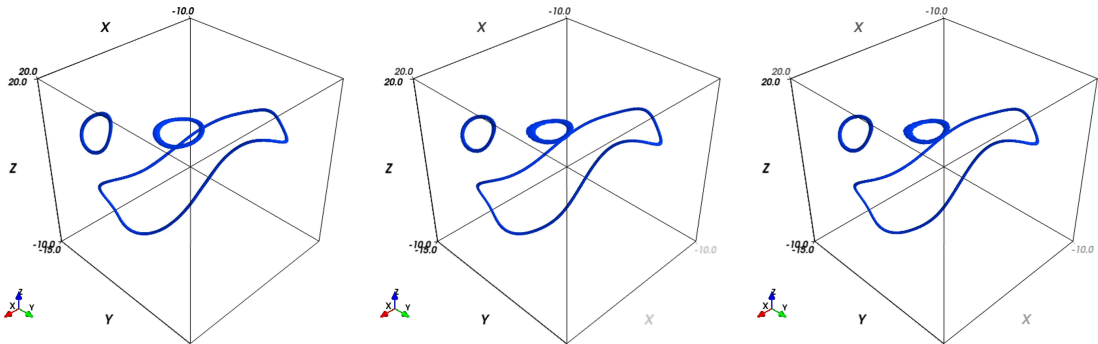


Figure 7: Initial condition as in [30], comparison between TSFP in $\Omega = [-20, 30] \times [-25, 25] \times [-20, 30]$ (left), FBTSFD (center) and TSFP in 2Ω (right) at $t=60$, $\rho=0.02$.

on the left) but within a doubled domain $\Omega = [-40, 60] \times [-50, 50] \times [-40, 60]$, with the same spatial resolution $\xi/3$ and the same time step $\tau = 1/80$ as in [30]. This comparison is carried out in order to evaluate the effect of the size of the computational domain on the Fourier approach. These parameters imply 300^3 degrees of freedom in the physical domain and a total of 8×300^3 in the computational domain. The initial condition at $t=0$ is the same for all cases, as shown in Fig. 4. As the simulation proceeds, the dynamics of the two rings is qualitatively very similar between the three cases (see Fig. 5, which refers to $t=20$) however for $t \geq 40$ differences emerge. In particular, an attentive inspection of the vortex tubes presented in Fig. 6 reveals that the Fourier approach in a limited domain (plot on the left) somehow slows down the ejection process of reconnected loops. This is due to the presence of “mirror” vortices necessary to make the initial condition (almost) periodic, as first done in [17]. In fact, it is well known that as two rings approach each other in a sort of head-on collision, they slow down considerably and increase their radius [18]. The effect of a truncated computational domain is clearly visible in Fig. 7. The plot on the left, when compared with the ones in the center and on the right, shows two small vortex rings moving slower than their counterparts in the other plots due to

a shorter distance from their mirror images. On the other hand, in a larger domain (plot on the right) the distance from the mirror rings is much larger and the effect is almost imperceptible. The present approach (central plot) does not suffer from this limitation as the physical domain extends to infinity. In order to achieve insensitivity to the domain size while keeping a reasonable spatial resolution ($\xi/3$), the number of degrees of freedom required by TSFP should increase considerably and may become critical, due to the mirroring needed in all three directions.

5.3.2 Mass, energy, and momentum variations

In Section 2 we have shown that under certain hypothesis ($\nabla\psi(x,t)\rightarrow 0$ and $|\psi(x,t)|^2\rightarrow 1$ for $|x|\rightarrow\infty$) which are verified for closed vortex loops as those presented in Figs. 4–7, time derivatives of mass (2.2), energy (2.4), and momentum (2.8) go to zero.

Fig. 8 summarizes mass (2.1), energy (2.3), and momentum (2.7) variations in the case of two linked vortex rings starting from the same initial condition as in [30]. Red symbols identify time splitting Fourier pseudospectral approach (TSFP). It should be noted that the integrals referring to TSFP are computed in the physical domain because in the mirrored domain their values should be zero for the reasons mentioned in Section 2. Empty circles refer to the simulation studied in [30], whereas stars denote the same simulation in a doubled domain, i.e. in $\Omega=[-40,60]\times[-50,50]\times[-40,60]$ with the same spatial resolution $\xi/3$, and the same time step $\tau=1/80=0.0125$. Since in this case there are 300^3 degrees of freedom in the physical domain, which become 8×300^3 in the computational domain due to mirroring in each spatial direction, the output file is very large and only few outputs were saved ($t=0, t=20, t=40$ and $t=60$). Blue symbols denote the present approach based on free boundary conditions time splitting finite-differences (FBTSFD). In this case, the integrals are computed in the whole transformed computational domain $(-1,1)^3$ or in a subdomain corresponding to $\Omega=[-L,L]^3$ in the physical domain. In Fig. 8 we report the relative variations with respect of the initial values of mass and energy (top row) and momentum (bottom row).

As known, the TSFP conserves discrete mass exactly [3], up to machine precision, whereas the FBTSFD approach does not. However, the relative variation shown in Fig. 8 for FBTSFD, top-left, as $L\rightarrow\infty$ at $t=60$, after 3000 time steps, is $9.49\cdot 10^{-9}$, thus extremely small. We also investigated how mass, energy, and momentum change in a finite cube. From the top-left plot of Fig. 8 it is clear that mass is by no means conserved in a small cube ($L<70$), and indeed there are no physical reasons for conservation to occur as mass can increase or decrease due to the motion of vortices. On a very large domain, as $L\rightarrow\infty$, which is insensitive to vortices motion, the relative variation goes to zero. For these reasons, the fact that TSFP conserves mass exactly on *any* computational domain is not necessarily a good feature, being conservation of mass unphysical in a domain too small.

The top-right plot of Fig. 8 shows that for none of the approaches the relative variation of energy goes to zero, however FBTSFD seems to perform a little better than TSFP as $L\rightarrow\infty$. The curves that grow very fast with time refer to the computation of energy on finite domains, where there are no physical reasons for energy to be conserved. The

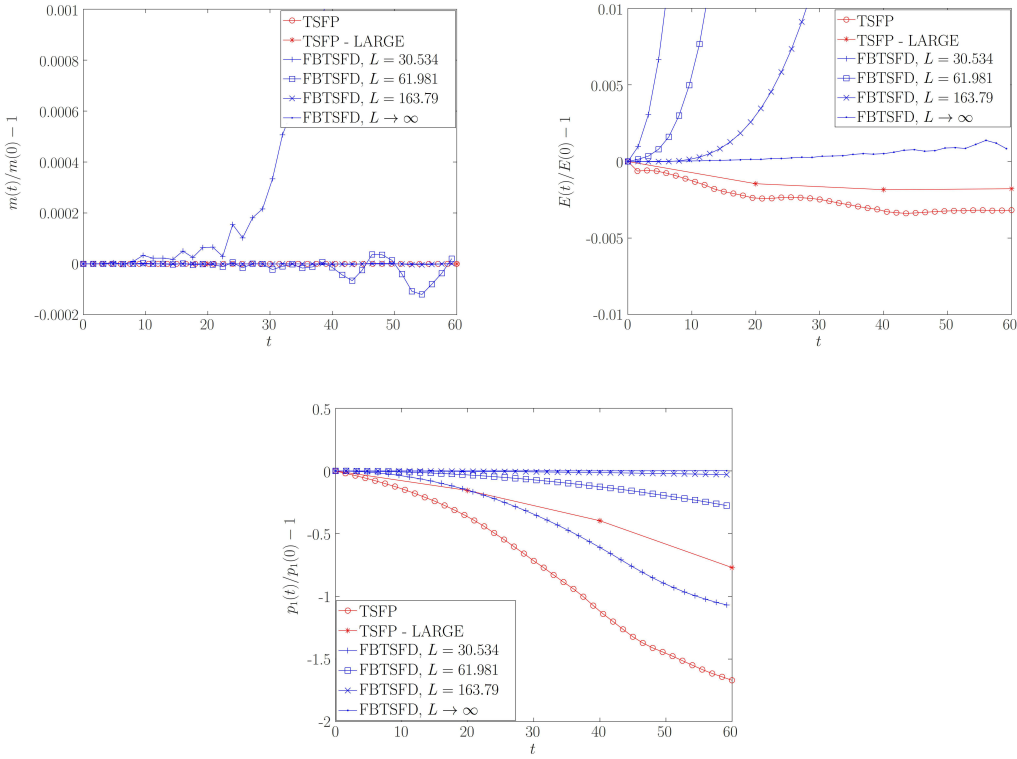


Figure 8: Computed relative variation of mass $m(t)/m(0) - 1$ (top left), of energy $E(t)/E(0) - 1$ (top right), and of momentum along x_1 $p_1(t)/p_1(0) - 1$ (bottom).

two simulations available for TSFP show that conservation of energy gets better as the computational domain increases.

As far as momentum is concerned, the bottom plot of Fig. 8 reports only the first component of \mathbf{p} (which is the largest together with the third component) and shows that the FBTSFD approach guarantees a much smaller relative variation than TSFP in $[-L, L]^3$ as $L \rightarrow \infty$.

The large variations in energy and momentum that characterize the TSFP approach decrease as the computational domain enlarges. Thus one might think that conservation of these quantities can be restored by using very large domains. However, in order to ensure reasonable spatial and time steps, employing large domains would result in memory requirements easily unbearable and in possible unaffordable computational times.

We can conclude that the new approach FBTSFD mimics the physics of GPE in a much easier way than TSFP thanks to the change of coordinates presented in Section 3 which maps the infinite domain $(-\infty, \infty)^3$ into the finite domain $(-1, 1)^3$.

5.3.3 Dynamics of orthogonal straight vortices

The reconnection between two orthogonal quantum vortices has been one of the first configurations studied [17]. In Fig. 9 we compare new results with those available for TSFP [29]. Qualitatively they look very similar, however there are two main differences. The first one is the dependence of TSFP on the simulation domain. Due to the presence of mirror vortices, straight vortex lines always hit the boundaries normally, therefore if the computational domain is relatively small, like in Fig. 9, top row, where it is $[-20, 20]^3$, vortex lines are limited in their dynamics. On the contrary, the new free boundary method (bottom row) allows vortex lines to move freely. The discretization for the TSFP approach is made of 100^3 points in the physical domain and a total of $8 \cdot 100^3$ degrees of freedom in the mirrored computational domain. The number of discretization points for the new approach is 167^3 . Together with the choice $\alpha = (15, 15, 15)$, we have an average spatial grid size in $[-20, 20]^3$ equivalent to the one in the Fourier pseudospectral method, that is 0.4. The time step was fixed to 0.1. We report in Table 3 the results. The new method requires a much smaller total number of discretization points and it is slightly faster than TSFP which, for this particular experiment, needs the mirroring along

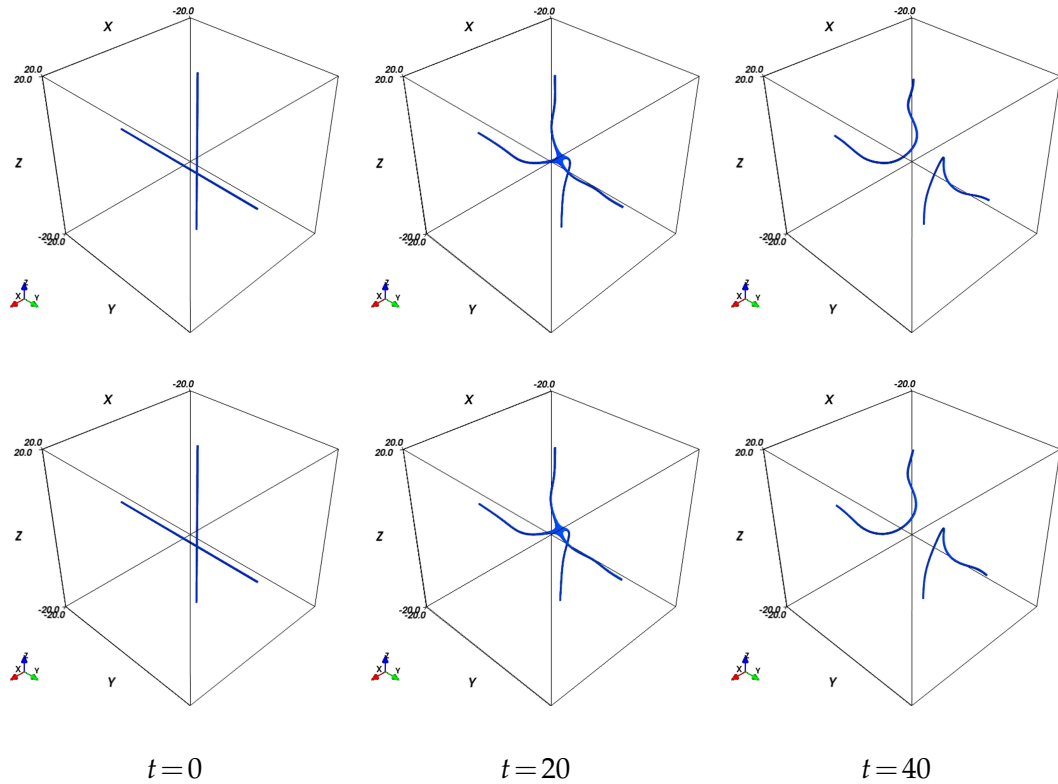


Figure 9: Orthogonal straight vortices, comparison between TSFP (top, see Fig. 6 in [29]) and FBTSFD (bottom) at different simulation time, $\rho = 0.02$.

Table 3: Degrees of freedom and elapsed computational times for the experiment with two orthogonal vortices.

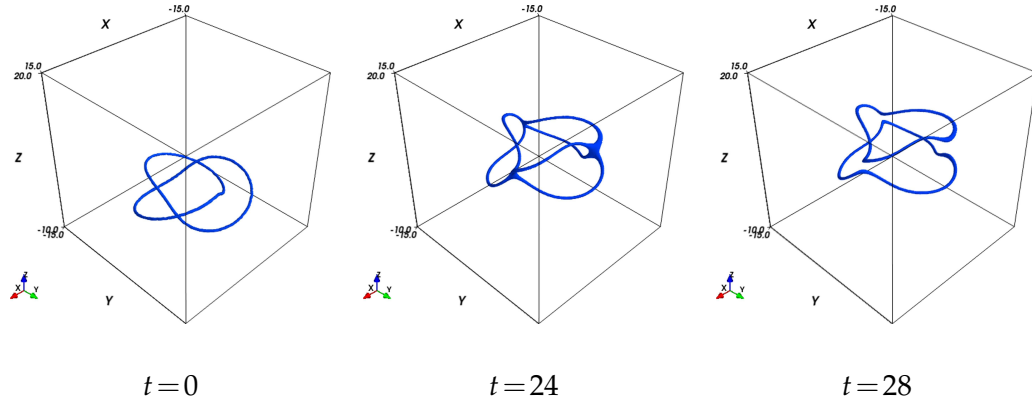
method	d.o.f.	CPU time (s.)
FBTSFD	167^3	81.24
FFT	$8 \cdot 100^3$	88.69

each space direction.

The second difference is the conservation of momentum (plots not reported). As seen in Fig. 8 for the case of linked rings, TSFP does not conserve momentum at all, whereas FBTSFD does it quite well.

5.3.4 Dynamics of torus knots

We have carried out tests for more complex vortex lines such as the torus knots presented in [31]. Fig. 10 collects three snapshots at different simulation time t for the initial condition described in Section 5.1 in the case of the torus knot \mathcal{T}_{23} . In Fig. 11 we report the time evolution of the torus knot \mathcal{T}_{25} , which reconnects earlier than \mathcal{T}_{23} as already observed in previous works [31].

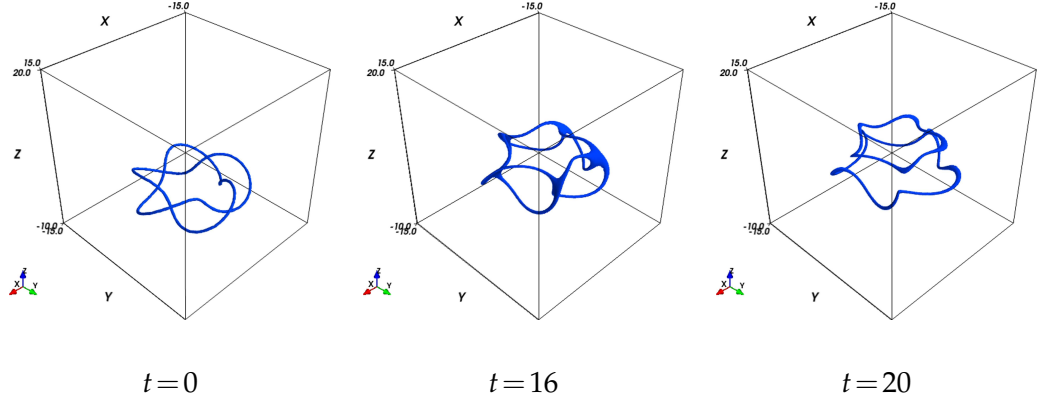
Figure 10: Dynamics of the torus knot \mathcal{T}_{23} at different simulation time, $\rho = 0.02$.

5.4 Simulations in one dimension

We report two one-dimensional cases to show the flexibility of the new approach, which is not limited to vortical structures but can be extended to more general dynamics.

5.4.1 One-dimensional dark solitons

We reproduce with our code the experiments described in [15, § 4.1], in which MSD boundary conditions are used. The one-dimensional nonlinear Schrödinger equation (1.1)

Figure 11: Dynamics of the torus knot \mathcal{T}_{25} at different simulation time, $\rho = 0.02$.

is written in the form

$$i\psi_t + \psi_{xx} - |\psi|^2\psi = 0$$

for which

$$\psi(x,t) = \tanh\left[\frac{\sqrt{2}}{2}(x-ct)\right] \exp\left(i\left[\frac{c}{2}x - \left(1 + \frac{c^2}{4}\right)t\right]\right) \quad (5.3)$$

is a comoving dark soliton solution. Clearly, $|\psi(x,t)|$ tends to 1 as $|x| \rightarrow \infty$.

The first experiment is with the “stationary” soliton corresponding to $c = 0$. Despite the name, the phase of the solution changes in time. We discretize the transformed domain $(-1,1)$ with $M = 503$ inner points. By choosing $\alpha = 5$, the average spatial grid size in the physical domain $(-25,25)$ is about 0.11. We run the numerical integration up to the final time $T = 50$ with 10000 time steps and measure the maximum errors in the real and imaginary parts of ψ after each time step over the length of the simulation. We find an average error of about $1.2 \cdot 10^{-6}$ for both the real and the imaginary parts. For this experiment, we tested the logarithmic map (3.3) with $\alpha = 10$. We obtained similar results, with average errors for the real and the imaginary parts around $1.3 \cdot 10^{-6}$. These are very much comparable with the error shown in [15, Fig. 4.1], where for a domain $(-25,25)$, a spatial grid size 0.1 and 10000 time steps, the error denoted by “average max error of $\Re(\psi)$ and $\Im(\psi)$ ” is between 10^{-6} and 10^{-5} .

In the second experiment the soliton travels with velocity $c = 0.5$. We discretize the transformed domain $(-1,1)$ with $M = 755$ inner points. By choosing $\alpha = 50$ we obtain an average spatial grid size in the physical domain $(-25,50)$ of about 0.25. The average errors for the real and the imaginary parts at time $T = 50$ after 10000 time steps are around $1.2 \cdot 10^{-4}$. For this experiment, we tested the logarithmic map (3.3) with the same value of $\alpha = 50$. The average errors for the real and the imaginary parts were below $8.31 \cdot 10^{-4}$. These are slightly larger than the error shown in [15, Fig. 4.2] for a very similar setting, which is below 10^{-5} . We can conclude that the present method can be satisfactorily employed for this type of simulations, after that the MSD was claimed to be “the only

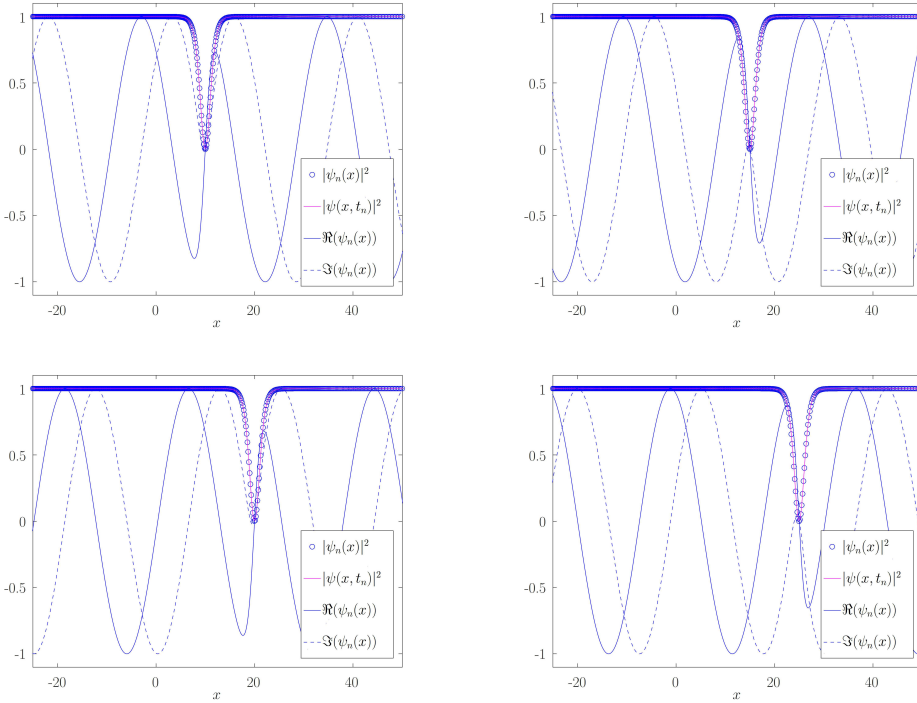


Figure 12: Behavior of the numerical $|\psi_n(x)|^2$ and exact (5.3) densities, and the real and imaginary parts of $\psi_n(x)$ at $t_n = 20, 30, 40, 50$, respectively.

simple-to-implement boundary condition that can handle such a comoving backflow''. Plots of the behavior of $\psi_n(x)$ are reported in Fig. 12. It is clear that, in this case, homogeneous Neumann conditions for $\psi(x, t)$ (that is for its real and imaginary part) at the boundaries of $(-25, 50)$ would have been completely unnatural.

5.4.2 Breathing of the ground state of a BEC

The method here proposed works very well also for the particular case of vanishing boundary conditions, used to simulate the dynamics of bright structures in Bose–Einstein condensates. We consider the following one-dimensional equation with a harmonic trap potential

$$\begin{cases} i\psi_t = -\frac{1}{2}\psi_{xx} + \frac{V(x)}{2}\psi + |\psi|^2\psi, & V(x) = \frac{x^2}{2}, \\ \psi(x, 0) = \psi_0(x). \end{cases} \quad (5.4)$$

The initial solution $\psi_0(x)$ is taken as the ground state of a similar equation, with a different frequency in the potential, namely

$$i\psi_t = -\frac{1}{2}\psi_{xx} + V(x)\psi + |\psi|^2\psi, \quad \|\psi(\cdot, t)\|_{L^2}^2 = 1. \quad (5.5)$$

We recall that the ground state is the solution in the form $\psi(x,t) = \phi(x)e^{-i\ell t}$, where $\phi: (-\infty, +\infty) \rightarrow \mathbb{R}$, $\ell \in \mathbb{R}$, with minimal energy

$$E(\psi) = E(\phi) = \int_{-\infty}^{+\infty} \left[\frac{1}{2} \phi_x^2(x) + V(x) \phi^2(x) + \frac{1}{2} \phi^4(x) \right] dx.$$

The dynamics of a ground state which is left to evolve with a different trap potential is called *breathing* (see [16]).

The most common technique to solve Eq. (5.4) is the TSFP method. In fact, due to the vanishing boundary conditions, the truncation of the domain with the imposition of the artificial periodic boundary conditions does not perturb the dynamics too much.

For the computation of the ground state several possibilities are available (see, again, [3]). The most common is probably the *imaginary time* method. Time t in Eq. (5.5) is substituted with it and the resulting parabolic equation is discretized in space, by Fourier decomposition, and integrated in time. After each time step, the wavefunction $\psi_n(x)$ is normalized. Here we prefer to consider the direct minimization of the energy functional performed in [10], after a decomposition into Hermite functions of the wavefunction. In fact, for the present method it is necessary to evaluate the initial solution at points $X^j \in (-\infty, \infty)$ which correspond to the discretization point $Y^j \in (-1, 1)$ through relations (3.2). If we used the imaginary time method with the TSFP method, the initial solution would have been affected from the beginning by an artificial periodicity in a truncated domain.

For the comparison with the classical TSFP method, the domain is truncated to $[-20, 20]$ and discretized with $M = 200$ points. A total amount of 10000 time steps are performed up to a final time $T = 46.3$, chosen in order to simulate ten recurrences of the density (see Fig. 13). For this experiment, the initial mass is equal to one and we can numerically verify its conservation (2.2). By using the trapezoidal rule (which is a Gaussian formula for trigonometric polynomials), we find that the average of the errors

$$|\|\psi(\cdot, t_n)\|_{L^2}^2 - \|\psi(\cdot, t_0)\|_{L^2}^2|$$

measured after each time step t_n is $4.60 \cdot 10^{-13}$. When comparing the final density $\rho = |\psi|^2$ at $x = -20$ to its initial value, we found $4.30 \cdot 10^{-30}$ instead of $6.61 \cdot 10^{-142}$.

With the FBTSFD method, we use $M = 203$ inner points and $\alpha = 5$, which give an average spatial grid size of 0.23 in the physical domain $(-20, 20)$. For the computation of the mass, we use the three-point open composite Milne's rule for

$$\int_{-\infty}^{\infty} |\psi(x, t_n)|^2 dx = \int_{-1}^1 |\eta(y, t_n)|^2 \frac{\pi \alpha}{1 + \cos(\pi y)} dy,$$

whose precision is $\mathcal{O}(h^5)$. We find an average error of $5.14 \cdot 10^{-9}$. The final value of $|\psi|^2$ at $-1.99 \cdot 10$ (the point X^j closest to -20) is $4.75 \cdot 10^{-45}$. The larger error in the mass preservation is due to the fact that the discrete mass is conserved up to an error depending on the space discretization error, as already observed in Section 4. On the other hand, the TSFP method would preserve the initial mass by construction also in extremely small domain,

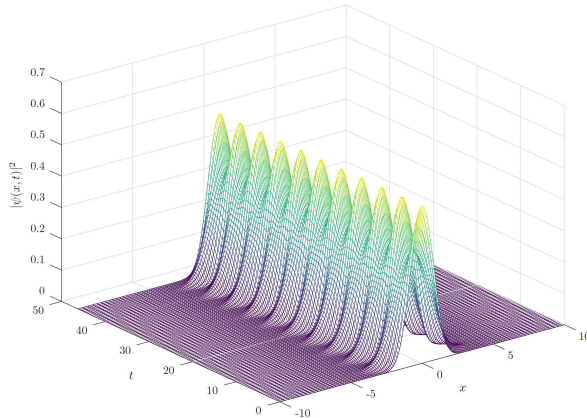


Figure 13: Absolute value of the solution of Eq. (5.4) (truncated in $x \in [-10, 10]$) with initial solution given by the ground state of Eq. (5.5) (*breathing*).

such as $[-1,1]$, where the physical experiment would exhibit an oscillatory behavior of the mass. The new method, however, preserves the vanishing boundary conditions much better than TSFP.

We also tested the MSD code[§] as implemented in [14]. For comparable values of the spatial grid size ranging from 0.25 to 0.1 it was not possible to perform the simulation, because very soon the code returned a vector of NaNs as solution. For a step size of 0.05 (and time step size automatically chosen equal to $2.1 \cdot 10^{-3}$ by the code), the method shows a very good conservation of the discrete mass computed by Simpson's rule, with an average error of $5.50 \cdot 10^{-14}$. The value of the density at $x = -20$ is $6.93 \cdot 10^{-122}$. For values of the spatial grid size smaller or equal to 0.025 the solution shows the problem already highlighted.

6 Conclusions

We have tackled the problem of simulating the behavior of a boundary condition of type $|\psi|^2 = B$, $B > 0$, for the Gross–Pitaevskii equation in an unbounded domain. This is a critical concern when dealing with the dynamics of dark structures and their possible reconnections in a background density whose value at infinity goes to one. We have solved the issue by rescaling the spatial variables and mapping the unbounded physical space \mathbb{R}^3 into the bounded domain $(-1,1)^3$. The governing equation is then discretized by 4th-order finite differences. As far as time integration is concerned, we have implemented both splitting and Runge–Kutta schemes and described their advantages and disadvantages. For the linear part in splitting methods, in particular, we have developed a very

[§]NLSEmagic1D version 020 available at <http://www.nlsemagic.com/>.

fast and accurate approximation of the action of the matrix exponential, taking into account the special Kronecker structure of the matrix.

Tests on the preservation of the single straight vortex show a relative error smaller than that observed using a classical Fourier pseudospectral approach on a finite domain, and at a much cheaper computational cost. In both cases, when performing a long time integration, we observe huge errors when the time steps are larger than a certain threshold related to the spatial discretization. In these situations, the solution does not diverge (as it happens with the Runge–Kutta), but the vortical structure is completely lost.

Previous results have been reproduced in both one- and three-dimensional cases. Comparisons with the pseudospectral approach on a finite three-dimensional domain made clear that the domain size plays a critical rôle in the correct dynamics of vortical structures and in the time evolution of global quantities such as mass, energy and momentum, whereas the new approach, for which the spatial variables extend up to infinity, is insensitive to this issue. After rewriting the time derivatives of these quantities in terms of boundary integrals of the wavefunction or of its spatial derivatives, we checked their numerical variations (in time) relative to their initial values. We observed that the fact that mass is always preserved in the pseudospectral context is not always a good feature, especially if the computational domain is too small. Moreover, for initial conditions that should preserve momentum, such as two linked rings, the pseudospectral approach needs a very large computational domain to show acceptable time variations, which could result in memory requirements easily unbearable and in possible unaffordable computational times. On the other hand, the free boundary approach confirms the theoretical expectation without any particular computational effort.

Other numerical tests in the one-dimensional case reproduce known results and prove the versatility of the free boundary approach. Numerical simulations of dark solitons, for which Modulus Square Dirichlet was claimed to be “the only simple-to-implement boundary condition that can handle such a comoving backflow”, provide errors comparable to existing results as well as breathing of the ground state of a BEC, for which vanishing boundary conditions are typically employed, does.

Like in the NLSEmagic code, the computational efficiency of the time integration by the splitting method could be further improved, for instance, by GPU-accelerated MEX files for the implementation of the action of the matrix exponential. Furthermore, we plan to use the FBTSD method for more complicate equations, such as the linear or nonlinear Schrödinger equation with vorticity (see [8, 9]).

Acknowledgments

The authors cordially thank Dr. Ronald M. Caplan for providing support on the NLSEmagic code. The authors would like to thank the Italian Ministry of Instruction, University and Research (MIUR) to support this research with funds coming from PRIN Project 2017 (No. 2017KKJP4X entitled “Innovative numerical methods for evolutionary partial differential equations and applications”).

A Derivation of time derivatives of mass, energy and momentum

From GPE (1.3) and its complex conjugate we have

$$\psi_t = \frac{i}{2} \nabla^2 \psi + \frac{i}{2} (1 - |\psi|^2) \psi, \quad (\text{A.1a})$$

$$\bar{\psi}_t = -\frac{i}{2} \nabla^2 \bar{\psi} - \frac{i}{2} (1 - |\psi|^2) \bar{\psi}, \quad (\text{A.1b})$$

$$\nabla \psi_t = \frac{i}{2} \nabla (\nabla^2 \psi) - \frac{i}{2} \nabla (|\psi|^2) \psi + \frac{i}{2} (1 - |\psi|^2) \nabla \psi, \quad (\text{A.1c})$$

$$\nabla \bar{\psi}_t = -\frac{i}{2} \nabla (\nabla^2 \bar{\psi}) + \frac{i}{2} \nabla (|\psi|^2) \bar{\psi} - \frac{i}{2} (1 - |\psi|^2) \nabla \bar{\psi}. \quad (\text{A.1d})$$

From the wavefunction written as $\psi = \sqrt{\rho} e^{iS}$, we have

$$\nabla \psi = \frac{\nabla \rho}{2\sqrt{\rho}} e^{iS} + \sqrt{\rho} e^{iS} i\mathbf{u},$$

where $\mathbf{u} = \nabla S$, and thus

$$\psi \nabla \bar{\psi} = \sqrt{\rho} e^{iS} \left[\frac{\nabla \rho}{2\sqrt{\rho}} e^{-iS} - \sqrt{\rho} e^{-iS} i\mathbf{u} \right] = \frac{\nabla \rho}{2} - \rho i\mathbf{u}, \quad \bar{\psi} \nabla \psi = \frac{\nabla \rho}{2} + \rho i\mathbf{u}.$$

Therefore

$$\psi \nabla \bar{\psi} - \bar{\psi} \nabla \psi = -2\rho i\mathbf{u} \implies \rho \mathbf{u} = \frac{i}{2} (\psi \nabla \bar{\psi} - \bar{\psi} \nabla \psi) = \Im(\bar{\psi} \nabla \psi). \quad (\text{A.2})$$

A.1 Mass

The total mass on a bounded domain $\Omega \subset \mathbb{R}^3$ is defined by

$$m_\Omega(t) = \int_{\Omega} |\psi|^2 dV.$$

By considering Eqs. (A.1a) and (A.1b), it is easy to derive

$$\begin{aligned} m'_\Omega(t) &= \frac{d}{dt} \left(\int_{\Omega} \psi \bar{\psi} dV \right) = \int_{\Omega} \psi_t \bar{\psi} + \psi \bar{\psi}_t dV \\ &= \frac{i}{2} \int_{\Omega} [\nabla \cdot (\bar{\psi} \nabla \psi - \psi \nabla \bar{\psi})] dV = \int_{\Omega} \Im[\nabla \cdot (\psi \nabla \bar{\psi})] dV. \end{aligned} \quad (\text{A.3})$$

By employing the divergence theorem, we finally have

$$m'_\Omega(t) = \Im \left(\int_{\partial\Omega} \psi (\nabla \bar{\psi} \cdot \hat{\mathbf{n}}) dS \right). \quad (\text{A.4})$$

A.2 Energy

Let us define $F_\Omega(t)$ as

$$F_\Omega(t) = E_\Omega(t) - \frac{1}{4} \int_\Omega dV.$$

We have

$$\begin{aligned} E'_\Omega(t) &= F'_\Omega(t) = \frac{1}{2} \int_\Omega \nabla \psi_t \cdot \nabla \bar{\psi} dV + \frac{1}{2} \int_\Omega \nabla \psi \cdot \nabla \bar{\psi}_t dV \\ &\quad - \frac{1}{2} \int_\Omega \psi_t \bar{\psi} dV - \frac{1}{2} \int_\Omega \psi \bar{\psi}_t dV \\ &\quad + \frac{1}{2} \int_\Omega |\psi|^2 \psi_t \bar{\psi} dV + \frac{1}{2} \int_\Omega |\psi|^2 \psi \bar{\psi}_t dV \\ &= \Re \left[\int_\Omega \nabla \psi \cdot \nabla \bar{\psi}_t dV - \int_\Omega (1 - |\psi|^2) \psi \bar{\psi}_t dV \right]. \end{aligned} \quad (\text{A.5})$$

Now, we take Eq. (A.1a) written in the form

$$i\psi_t = -\frac{1}{2} \nabla^2 \psi - \frac{1}{2} (1 - |\psi|^2) \psi,$$

we multiply by $\bar{\psi}_t$, integrate, and apply the first Green's identity. We have

$$\begin{aligned} i \int_\Omega |\psi_t|^2 &= -\frac{1}{2} \int_\Omega \nabla^2 \psi \bar{\psi}_t dV - \frac{1}{2} \int_\Omega (1 - |\psi|^2) \psi \bar{\psi}_t dV \\ &= -\frac{1}{2} \int_{\partial\Omega} \nabla \psi \cdot \hat{n} \bar{\psi}_t dS + \frac{1}{2} \int_\Omega \nabla \psi \cdot \nabla \bar{\psi}_t dV \\ &\quad - \frac{1}{2} \int_\Omega (1 - |\psi|^2) \psi \bar{\psi}_t dV. \end{aligned}$$

Hence, by comparing with (A.5), we get

$$2\Re \left[i \int_\Omega |\psi_t|^2 + \frac{1}{2} \int_{\partial\Omega} \nabla \psi \cdot \hat{n} \bar{\psi}_t dS \right] = \Re \left[\int_{\partial\Omega} \nabla \psi \cdot \hat{n} \bar{\psi}_t dS \right] = E'_\Omega(t).$$

We insert $\bar{\psi}_t$ to get

$$\begin{aligned} E'_\Omega(t) &= \Re \left[-\frac{i}{2} \int_{\partial\Omega} \nabla \psi \cdot \hat{n} \nabla^2 \bar{\psi} dS - \frac{i}{2} \int_{\partial\Omega} \nabla \psi \cdot \hat{n} (1 - |\psi|^2) \bar{\psi} dS \right] \\ &= \Im \left[\frac{1}{2} \int_{\partial\Omega} \nabla \psi \cdot \hat{n} \nabla^2 \bar{\psi} dS + \frac{1}{2} \int_{\partial\Omega} \nabla \psi \cdot \hat{n} (1 - |\psi|^2) \bar{\psi} dS \right]. \end{aligned} \quad (\text{A.6})$$

A.3 Momentum

The linear momentum is defined by

$$\mathbf{P}_\Omega(t) = \int_\Omega \rho \mathbf{u} dV,$$

which can be recast in terms of the wavefunctions (see (A.2)) as

$$\mathbf{P}_\Omega(t) = \Im \left(\int_\Omega \bar{\psi} \nabla \psi dV \right).$$

We wish to compute the change of linear momentum in time, i.e.

$$\mathbf{P}'_\Omega(t) = \Im \left(\int_\Omega (\bar{\psi}_t \nabla \psi + \bar{\psi} \nabla \psi_t) dV \right).$$

By taking (A.1b) and (A.1c), we have

$$\begin{aligned} \mathbf{P}'_\Omega(t) &= \Im \left(\int_\Omega (\bar{\psi}_t \nabla \psi + \bar{\psi} \nabla \psi_t) dV \right) \\ &= -\frac{1}{2} \Re \left(\int_\Omega (\nabla^2 \bar{\psi} \nabla \psi + (1 - |\psi|^2) \bar{\psi} \nabla \psi \right. \\ &\quad \left. - \bar{\psi} \nabla (\nabla^2 \psi) + |\psi|^2 \nabla (|\psi|^2) - (1 - |\psi|^2) \bar{\psi} \nabla \psi) dV \right) \\ &= -\frac{1}{2} \Re \left(\int_\Omega \left(\nabla^2 \bar{\psi} \nabla \psi - \bar{\psi} \nabla (\nabla^2 \psi) + \nabla \left(\frac{1}{2} |\psi|^4 \right) \right) dV \right). \end{aligned}$$

We observe that, by exchanging the order of differentiation, we have

$$\nabla(\nabla^2 \psi) = \begin{bmatrix} (\psi_{x_1 x_1})_{x_1} + (\psi_{x_2 x_2})_{x_1} + (\psi_{x_3 x_3})_{x_1} \\ (\psi_{x_1 x_1})_{x_2} + (\psi_{x_2 x_2})_{x_2} + (\psi_{x_3 x_3})_{x_2} \\ (\psi_{x_1 x_1})_{x_3} + (\psi_{x_2 x_2})_{x_3} + (\psi_{x_3 x_3})_{x_3} \end{bmatrix} = \begin{bmatrix} \nabla^2(\psi_{x_1}) \\ \nabla^2(\psi_{x_2}) \\ \nabla^2(\psi_{x_3}) \end{bmatrix} = \nabla^2(\nabla \psi),$$

thus the integral

$$\int_\Omega (\nabla^2 \bar{\psi} \nabla \psi - \bar{\psi} \nabla (\nabla^2 \psi)) dV$$

can be written component-wise as

$$\int_\Omega (\psi_{x_\ell} \nabla^2 \bar{\psi} - \bar{\psi} \nabla^2(\psi_{x_\ell})) dV, \quad \ell = 1, 2, 3.$$

By applying Green's second identity

$$\int_\Omega (f \nabla^2 g - g \nabla^2 f) dV = \int_{\partial\Omega} (f \nabla g - g \nabla f) \cdot \hat{\mathbf{n}} dS$$

to each of this integrals, where $\hat{\mathbf{n}}$ denotes the outward unit normal, we get

$$\int_{\Omega} (\psi_{x_\ell} \nabla^2 \bar{\psi} - \bar{\psi} \nabla^2 (\psi_{x_\ell})) dV = \int_{\partial\Omega} (\psi_{x_\ell} \nabla \bar{\psi} - \bar{\psi} \nabla (\psi_{x_\ell})) \cdot \hat{\mathbf{n}} dS, \quad \ell=1,2,3.$$

By recalling that, in general,

$$\int_{\Omega} \nabla f dV = \int_{\partial\Omega} f \hat{\mathbf{n}} dS, \quad (\text{A.7})$$

we also obtain

$$\int_{\Omega} \nabla \left(\frac{1}{2} |\psi|^4 \right) dV = \int_{\partial\Omega} \frac{1}{2} |\psi|^4 \hat{\mathbf{n}} dS.$$

In conclusion, since the last integral is certainly real ($|\psi|^4 \in \mathbb{R}$), we can recast the derivative of ℓ -th component of the momentum with respect to time as

$$p'_{\ell\Omega}(t) = -\frac{1}{2} \Re \left[\int_{\partial\Omega} (\psi_{x_\ell} \nabla \bar{\psi} - \bar{\psi} \nabla (\psi_{x_\ell}) + \mathbf{F}_\ell) \cdot \hat{\mathbf{n}} dS \right], \quad (\text{A.8})$$

where \Re denotes the real part of a complex quantity and $\mathbf{F}_\ell = |\psi|^4 \hat{\mathbf{e}}_\ell / 2$, $\hat{\mathbf{e}}_\ell$ being the unit vector along the ℓ -th direction.

References

- [1] D. G. Akhmetov. *Vortex Rings*. Springer-Verlag, Berlin Heidelberg, 1 edition, 2009.
- [2] A. H. Al-Mohy and N. J. Higham. A new scaling and squaring algorithm for the matrix exponential. *SIAM J. Matrix Anal. Appl.*, 31(3):970–989, 2009.
- [3] W. Bao and Y. Cai. Mathematical theory and numerical methods for Bose–Einstein condensation. *Kinet. Relat. Models*, 6(1):1–135, 2013.
- [4] W. Bao, Q. Tang, and Z. Xu. Numerical methods and comparison for computing dark and bright solitons in the nonlinear Schrödinger equation. *J. Comput. Phys.*, 235:423–445, 2013.
- [5] C. F. Barenghi and N. G. Parker. *A Primer on Quantum Fluids*. Springer, 2016.
- [6] N. G. Berloff. Padé approximations of solitary wave solutions of the Gross–Pitaevskii equation. *J. Phys. A: Math. Gen.*, 37:1617–1632, 2004.
- [7] J. P. Boyd. *Chebyshev and Fourier spectral methods*. DOVER Publications, Inc., second edition, 2000.
- [8] M. Caliari, G. Inverso, and L. M. Morato. Dissipation caused by a vorticity field and generation of singularities in Madelung fluid. *New J. Phys.*, 6:69, 2004.
- [9] M. Caliari, M. I. Loffredo, L. M. Morato, and S. Zuccher. Cubic nonlinear Schrödinger equation with vorticity. *New J. Phys.*, 10:123020, 2008.
- [10] M. Caliari and S. Rainer. GSGPEs-v1.1: a MATLAB code for computing the ground state of systems of Gross–Pitaevskii equations. *Comput. Phys. Commun.*, 247:106968, 2020.
- [11] M. Caliari and F. Zivcovich. On-the-fly backward error estimate for matrix exponential approximation by Taylor algorithm. *J. Comput. Appl. Math.*, 346:532–548, 2019.
- [12] M. Caliari and S. Zuccher. INFFT: Fast evaluation of 3d Fourier series in MATLAB with an application to quantum vortex reconnections. *Comput. Phys. Commun.*, 213:197–207, 2017.
- [13] M. Caliari and S. Zuccher. Reliability of the time splitting Fourier method for singular solutions in quantum fluids. *Comput. Phys. Commun.*, 222:46–58, 2018.

- [14] R. M. Caplan. NLSEmagic: Nonlinear Schrödinger equation multidimensional Matlab-based GPU-accelerated integrators using compact high-order schemes. *Comput. Phys. Commun.*, 184(4):1250–1271, 2013.
- [15] R. M. Caplan and R. Carretero-González. A modulus-squared Dirichlet boundary condition for time-dependent complex partial differential equations and its application to the nonlinear Schrödinger equation. *SIAM J. Sci. Comput.*, 36(1):A1–A19, 2014.
- [16] C. M. Dion and E. Cancès. Spectral method for the time-dependent Gross–Pitaevskii equation with a harmonic trap. *Phys. Rev. E*, 67:046706, 2003.
- [17] J. Koplik and H. Levine. Vortex Reconnection in Superfluid Helium. *Phys. Rev. Lett.*, 71(9):1375–1379, 1993.
- [18] T. T. Lim and T. B. Nickels. Instability in the reconnection in the head-on collision of two vortex rings. *Nature*, 357:225–227, 1992.
- [19] D. Proment, M. Onorato, and C. F. Barenghi. Vortex knots in a Bose–Einstein condensate. *Phys. Rev. E*, 85:036306, 2012.
- [20] G. W. Rayfield and F. Reif. Quantized vortex rings in superfluid helium. *Phys. Rev.*, 136:A1194–A1208, 1964.
- [21] P. H. Roberts and N. G. Berloff. The nonlinear Schrödinger equation as a model of superfluidity. In C. F. Barenghi, R. J. Donnelly, and W. F. Vinen, editors, *Quantized Vortex Dynamics and Superfluid Turbulence*, volume 571 of *Lecture Notes in Physics*, pages 235–257. Springer, Berlin Heidelberg, 2001.
- [22] P. H. Roberts and J. Grant. Motions in a Bose condensate. I. The structure of the large circular vortex. *J. Phys. A: Gen. Phys.*, 4:55–72, 1971.
- [23] M. W. Scheeler, D. Kleckner, D. Proment, G. L. Kindlmann, and W. T. M. Irvine. Helicity conservation by flow across scales in reconnecting vortex links and knots. *Proc. Natl. Acad. Sci. USA*, 111(43):15350–15355, 2014.
- [24] I. S. Sullivan, J. J. Niemela, R. E. Hershberger, D. Bolster, and R. J. Donnelly. Dynamics of thin vortex rings. *J. Fluid Mech.*, 609:319–347, 2008.
- [25] M. Thalhammer, M. Caliari, and C. Neuhauser. High-order time-splitting Hermite and Fourier spectral methods. *J. Comput. Phys.*, 228(3):822–832, 2009.
- [26] Y. Zhang, W. Bao, and Q. Du. The dynamics and interaction of quantized vortices in Ginzburg–Landau–Schrödinger equations. *SIAM J. Appl. Math.*, 67:1740–1775, 2007.
- [27] Y. Zhang, W. Bao, and Q. Du. Numerical simulation of vortex dynamics in Ginzburg–Landau–Schrödinger equation. *Eur. J. Appl. Math.*, 18:607–630, 2007.
- [28] S. Zuccher and M. Caliari. Accurate numerical determination of a self-preserving quantum vortex ring. *J. Phys. A: Math. Theor.*, 54(1):015301, 2021.
- [29] S. Zuccher, M. Caliari, A. W. Baggaley, and C. F. Barenghi. Quantum vortex reconnections. *Phys. Fluids*, 24(125108):1–21, 2012.
- [30] S. Zuccher and R. L. Ricca. Relaxation of twist helicity in the cascade process of linked quantum vortices. *Phys. Rev. E*, 95:053109, 2017.
- [31] S. Zuccher and R. L. Ricca. Momentum of vortex tangles by weighted area information. *Phys. Rev. E*, 100:011101(R), 2019.